A Picture of the Moon's Atmosphere

Brian Flynn and Michael Mendillo*

Atomic sodium is a useful tracer of the tenuous lunar atmosphere because of its high efficiency in scattering sunlight at the D_1 (5896 angstroms) and D_2 (5890 angstroms) wavelengths. In 1988, Earth-based instruments revealed the presence of sodium at a density of less than 50 atoms per cubic centimeter at lunar altitudes below 100 kilometers. Telescopic observations that are made with a coronograph technique to block out the disk of the moon allow a true picture of the circumlunar atmosphere to be obtained and show the presence of sodium out to a distance of several lunar radii. The distribution of sodium has a solar zenith angle dependence, suggesting that most of the sodium that reaches great altitudes is liberated from the moon's surface by solar photons (by heating or sputtering) or by solar wind impact, in contrast to a source driven by uniform micrometeor bombardment.

At the dawn of the 20th century, it was still an open question whether the moon had an atmosphere (*1*). Observations in the following decades constrained the possible extent and density of the moon's gaseous environment and, by the time of the Apollo landings, in situ measurements yielded an estimated surface density of less than 10^7 atoms per cubic centimeter (*2*). This value was poorly defined during the daytime because of gas escaping from the material of the lunar landers. The discovery of Na within an altitude of 100 km came as a surprise (*3, 4*) but was soon followed by further detection of Na at heights an order of magnitude higher—up to 70% of a lunar radius, R_m, above the equator at the limb (*5*).

The same spectroscopic techniques by which Na was discovered were also used to investigate its latitude dependence. Detection of Na above the polar regions (*3*), and consideration of its likely sources, pointed to the possible existence of a Na coma (*5*) formed in much the same way as gas escaping the weak gravitational attraction of a comet's nucleus. One set of recent observations has suggested that Na emission intensities at low altitudes above the equator are rather stable and are typically three to four times those found in polar regions (*6, 7*). These studies suggested that the amount of Na decreases more rapidly with altitude near the equator than at the poles (*7*). An earlier, independent set of observations (*8*) found that circumlunar Na emission levels at 50 km vary by less than a factor of 2 from the equator to the poles, and the falloff with altitude is more rapid near the poles than above the equator. Thus, the totality of published data from high-resolution spectroscopy made at a few single-point measurement positions close to the lunar surface (at altitudes $<1\ R_m$) has not yet produced an unambiguous morphology that can be used to test models with different temperatures and latitude dependencies for Na (*7–9*).

To obtain a global morphology for the lunar Na atmosphere, an imaging system that is capable of making observations at wide angles and low light levels is required. Such an instrument was developed to study Jupiter's great Na nebula (*10, 11*), and it was used subsequently in several imaging experiments to search for evidence of an extended lunar atmosphere (*12*). In the first attempt, a field-of-view (FOV)–offset technique was used in which the FOV was positioned east and west of the moon in order to prevent the moon's bright image from saturating the detector. This method showed that a Na coma extended to at least 5 R_m along the moon-sun line, with taillike structures out to 15 to 20 R_m in the anti-sunward direction (*13*).

The FOV-offset technique sacrificed spatial coverage at middle and polar latitudes in order to cope with high levels of scattered moonlight. A subsequent coronagraph mask technique, in which a black disk (light trap) was placed on the field lens of the telescope to block the central 1° of the FOV, proved successful in tests conducted at McDonald Observatory in fall 1991 and winter 1992. With the moon (diameter 0.5°) centered on the 1° occulting mask, no observations within 1 R_m of the surface are possible. Because this is the very region documented by all previous spectroscopic observations, a strategy was developed in which near-moon radial coverage was achieved by the merging of images taken with the moon's limb near the north-south-east-west points at the rim of the occulting mask. In each position, on- and off-band pictures were taken to capture Na and scattered light signatures, with a separate off-target set used to characterize telluric signals. The results of such a composite image made on 30 September 1991 (last quarter) are presented in Fig. 1.

From the original FOV-offset observation (20 February 1991), the total Na ($D_1 + D_2$) brightness levels along the radial direction to the sun were shown to be well represented by a power law, $I(r) = I_0 r^{-\alpha}$, where r is the distance from the center of the moon in R_m, I_0 is the equivalent brightness at the limb ($r = 1$), and $\alpha = 4$. Results from the 30 September 1991 observation (Fig. 1), as well as from a subsequent observation on 10 February 1992, are shown in Fig. 2. There is a consistent pattern in all the data sets, showing the r^{-4} structure to be representative of subsolar conditions over extended periods of time (12 months). This stable feature describes an essentially bound, although extended, atmosphere; a hemispherically symmetric atmosphere dominated by escape (*9*) would result in an r^{-1} radial intensity profile, such as exists for the extended Na nebula at Jupiter (*11*).

In the FOV-offset observations of 20 February 1991, lunar Na emissions were seen in tail lobes extending in the anti-sunward direction from the north and south polar regions (*13*). A region of reduced emission was seen directly behind the moon, consistent with the geometrical lunar shad-

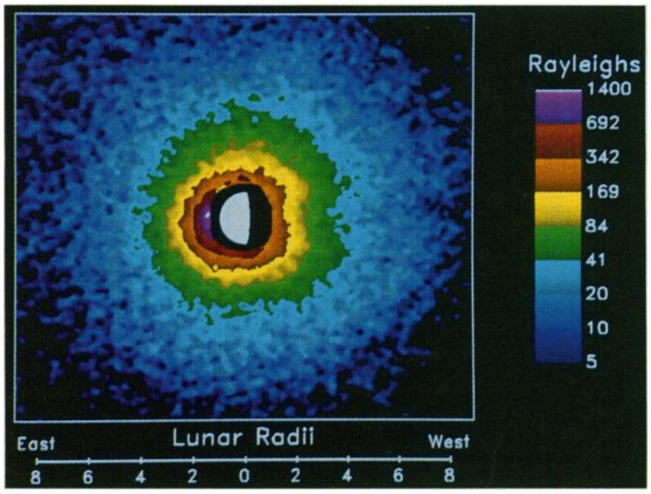

Fig. 1. Total Na emission ($D_1 + D_2$ line intensities) resulting from four separate images with the moon at the north-south-east-west points on a 1° occulting mask. The observations were made from 09:55 UT to 12:00 UT on 30 September 1991 at McDonald Observatory in Fort Davis, Texas. Stars in the individual frames, used to align the fields of view to create the composite, were removed during image processing.

Department of Astronomy and Center for Space Physics, Boston University, Boston, MA 02215.

*To whom correspondence should be addressed.

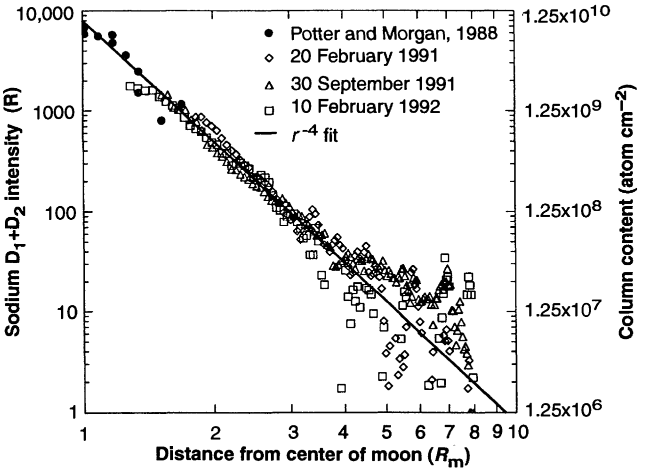

Fig. 2. Radial profile of the $D_1 + D_2$ intensities extracted from Fig. 1 along the sun-moon line shown in comparison with results from earlier and later data sets. All data sets are well represented by the same r^{-4} intensity power law.

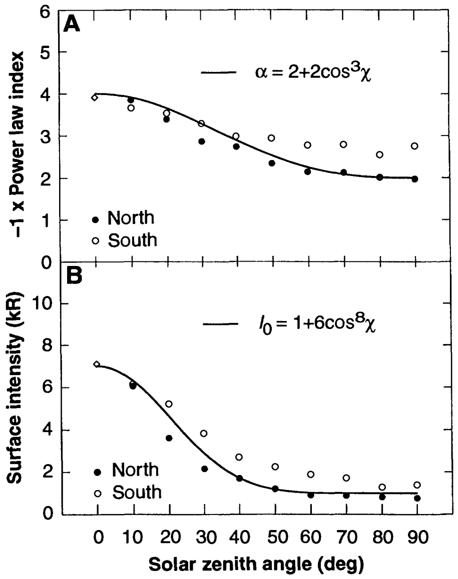

Fig. 4. (**A**) Solar zenith angle (~latitude) dependence of the power law index used to describe radial intensity behavior from subsolar to polar regions. (**B**) Solar zenith angle (~latitude) dependence of the equivalent surface brightness of Na ($D_1 + D_2$) derived from fits of radial intensities from subsolar to polar regions.

ow. The Na atoms in the moon's shadow are shielded from sunlight and therefore do not contribute to the cross-tail column of emission detected from Earth. In Fig. 1, the tail lobes and shadow effect are seen clearly in emission levels close to the moon. Scans of the image perpendicular to the sun-moon axis, normalized by the peak lobe brightness at each distance in the tail region, were averaged to yield the results shown in Fig. 3. The tail lobes and shadow effects are another permanent, although variable, feature of the lunar Na atmosphere. The lack of a truly extended tail morphology in Fig. 1 may be due to variations in the solar radiation pressure effect that reduced such features in September 1991 in comparison to their initial appearance in February 1991 (*14*, *15*), or to Na source fluctuations (6), or to atmospheric transparency effects over the 7-month period.

The sun-moon axis essentially strikes the equator at local noon for the first- and third-quarter moon. At that point, the zenith angle to the sun is zero. For other zenith angles along the noon meridian (χ = 0° to ± 90°), χ may be considered to represent latitude on the moon. The radial behavior of the Na brightness in Fig. 1 can be used, together with the power law formulation described above, to determine the best fit I_0 and α values that describe the full dayside coma. The results of such an analysis are presented in Fig. 4 and represent the major advance to come from the use of the occulting mask technique. There is a smooth decrease of the equivalent surface intensity (I_0) by a factor of 7 from the equator to the poles (Fig. 4B). There is a clear transition from an $\alpha = 4$ radial dependence near the equator to $\alpha = 2$ near the poles (Fig. 4A). Using a simple barometric law representation and assuming hemispheric symmetry, we find that the $\alpha = 4$ results correspond to a Na scale height (H) evaluated at the surface of approximately 1000 km (or $T = 4500$ K); the $\alpha = 2$ power law corresponds to H and T values that are twice as large. In either representation, there is a marked transition from a steep falloff at low latitudes to a more gradual one near the poles (*15*). The results portrayed in Fig. 4 support the hypothesis of a transition from an atmosphere dominated by a solar zenith angle–dependent source mechanism in subsolar regions to an atmosphere dominated by an isotropic mechanism near the poles (*7*).

The results of the image analysis portrayed above can be merged into an analytical description of the dayside lunar Na distribution:

$$I(r,\chi) = I_0 r^{-\alpha} \qquad (1)$$

where $I_0 = (1 + 6\cos^8\chi)$ and $\alpha = 2(1 + \cos^3\chi)$, I_0 is measured in kilorayleighs, r is distance in R_m, and χ is the solar zenith angle (latitude). Such a representation suggests that the isotropic source mechanism (presumably Na released by micrometeor impact) is a relatively weak component (15%) in comparison to the solar zenith angle–dependent mechanism (85%). The latter mechanism is presumably a combination of photo and thermal desorption driven by sunlight or possibly sputtering from solar wind impact, and its solar zenith angle dependence is surprisingly strong.

Finally, it should be emphasized that the imaging techniques used here capture Na features that extend beyond ~500 km above the surface and thus to the so-called hot component associated with Na ejection velocities near 2 km s^{-1} (or $T = 3000$ K) (*16*). A population of Na atoms thermally accommodated to surface conditions ($T \leq 400$ K or velocity ≤ 0.7 km s^{-1}) would not be expected to reach altitudes viewed by the imaging system (*7*). The global distribution of total Na near the surface would, therefore, be expected to be different from the high-altitude Na distribution portrayed in Figs. 1 and 4. Both regimes would also be expected to be variable, as evidenced by results in the existing literature.

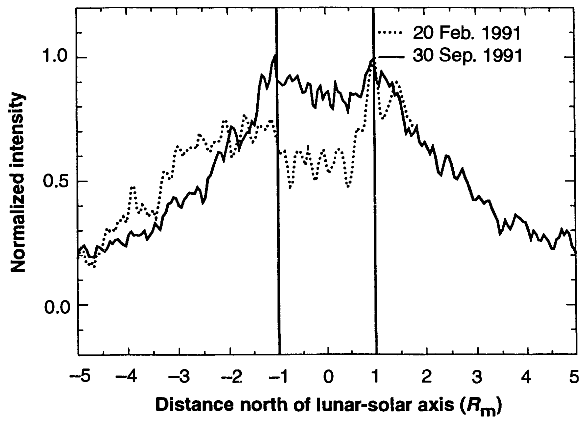

Fig. 3. Characterization of the moon's shadow effect on Na intensities in the antisolar direction. Average cross-tail profiles normalized by the peak brightness at each distance from the moon are shown for the observations in Fig. 1 and from the earlier FOV-offset observations (*13*).

REFERENCES AND NOTES

1. In *A Short History of Astronomy* (1898), reissued by Dover Publications, New York, 1961, Arthur Berry states (p. 383): "The question of a lunar atmosphere is more difficult: if there is air its

density must be very small, some hundredfold less than that of our atmosphere at the surface of the earth; but with this restriction there seems to be no bar to the existence of a lunar atmosphere of considerable extent, and it is difficult to explain certain observations without assuming the existence of some atmosphere."

2. T. Morgan and A. Stern, *Eos* 72, 225 (1991). In comparison to the Earth's total atmospheric density of ~10^{19} molecules per cubic centimeter at the surface, the lunar value is lower by a factor of 10^{-12}.
3. A. E. Potter and T. H. Morgan, *Science* **241**, 675 (1988).
4. A. Tyler, R. Kozlowski, D. Hunten, *Geophys. Res. Lett.* **15**, 1141 (1988).
5. The mean lunar radius (R_m) is 1738 km; Na was detected at ~1200 km by A. Potter and T. Morgan (*ibid.*, p. 1515).
6. D. Hunten, R. Kozlowski, A. Sprague, *ibid.* **18**, 2101 (1991).
7. A. Sprague, R. Kozlowski, D. Hunten, W. Wells, R. Grosse, *Icarus* **96**, 27 (1992).
8. A. Potter and T. Morgan, *Geophys. Res. Lett.* **18**, 2089 (1991).
9. T. Morgan and D. Shemansky, *J. Geophys. Res.* **96**, 1351 (1991).
10. M. Mendillo, J. Baumgardner, B. Flynn, *Nature* **348**, 312 (1990).
11. B. Flynn, M. Mendillo, J. Baumgardner, *Icarus* **99**, 115 (1992).
12. M. Mendillo, B. Flynn, J. Baumgardner, *Adv. Space Res.*, in press.
13. M. Mendillo, J. Baumgardner, B. Flynn, *Geophys. Res. Lett.* **18**, 2097 (1991).
14. W.-H. Ip, *ibid.*, p. 2093.
15. Detailed analysis and modeling of these and other image sets are under way: B. Flynn, unpublished results; W. Smyth, personal communication.
16. If the emergent Na velocity distribution is Maxwellian, the root mean square velocity $V_{rms} = (3kT/m)^{1/2}$ (m is mass) reduces to V (in kilometers per second) = $0.033\sqrt{T}$ (in kelvin).
17. This work was supported, in part, by a grant from the National Aeronautics and Space Administration Space Physics Division and by funds provided for the Center for Space Physics at Boston University. We are grateful for the assistance of J. Baumgardner, for discussion with A. Sprague and D. Hunten, and for the insightful comments of a referee. Both authors are Guest Observers at the McDonald Observatory, and we acknowledge the continued cooperation of observatory personnel in making these observations possible.

15 March 1993; accepted 20 May 1993

Relation Between Bond-Length Alternation and Second Electronic Hyperpolarizability of Conjugated Organic Molecules

Seth R. Marder,* Joseph W. Perry,* Grant Bourhill, Christopher B. Gorman, Bruce G. Tiemann, Kamjou Mansour

The solvent dependence of the second hyperpolarizability, γ, of a variety of unsaturated organic compounds has been measured by third harmonic generation at 1907 nanometers. It is seen that the measured γ is a function of solvent polarity. These solvent-dependent hyperpolarizabilities are associated with changes in molecular geometry from a highly bond-length alternated, polyene-like structure for a formyl-substituted compound in nonpolar solvents, to a cyanine-like structure, with little bond-length alternation, for a dicyanovinyl-substituted compound in polar solvents. By tuning bond-length alternation, γ can be optimized in either a positive or negative sense for polymethine dyes of a given conjugation length.

The development of materials with third-order optical nonlinearities has been the focus of much recent research (*1, 2*). Such materials are of interest for a variety of optical switching and processing applications. However, materials with sufficiently high nonlinearities for most of these applications have not yet been identified (*3*). In contrast to the relatively well-defined structure-property relationships (*1, 2, 4*) used to guide the design of molecules for second-order nonlinear optical applications, such relationships for third-order nonlinear optical chromophores are lacking (*5*). Theoretical and experimental studies (*4*) suggest that bond-length alternation, <Δ*r*> (defined as the difference between the average lengths of carbon-carbon single and double bonds in a polymethine chain) is a useful structural parameter to vary in attempts to optimize the first hyperpolarizability, β, for organic molecules. Recent semiempirical molecular orbital calculations support this hypothesis and predict that trends for the second hyperpolarizability, γ, are associated with bond-length alternation (*6*). For example, electric field–dependent calculations of geometry and second hyperpolarizability indicate that for highly bond-length alternated molecules, such as polyenes, γ is positive; as a function of increasing polarization and decreasing <Δ*r*>, γ first increases, peaks in a positive sense, decreases, crosses through zero and ultimately peaks in a negative sense at the cyanine-limit of zero bond-length alternation (Fig. 1). To develop structure-property relationships for γ and to test these predictions, we examined a series of molecules whose bond-length alternation spans the range accessible to organic molecules containing polymethine chains.

We report γ values for a set of molecules (**1** to **4** and **6**, Fig. 2) ranging from polyenes, for which the bond-length alternation equals 0.11 Å (as determined crystallographically, from diphenyl octatetraene (*7*) and octatetraene (*8*) to cyanines, for which <Δ*r*> is essentially zero, again determined crystallographically (*9, 10*). In order to tune the bond-length alternation from the polyene limit to the cyanine limit, we used two donor-acceptor polyenes with acceptors of differing strength in solvents ranging from nonpolar to highly polar. Such solvent-dependent changes in structure can be understood in terms of simple resonance structure arguments (*11*). The ground state of a polymethine dye can be described in terms of contributions of two limiting charge transfer resonance structures (Fig. 2). The equilibrium structure of the ground state represents a weighted average of the limiting resonance structures and approaches a bond-equivalent structure for an equal mixture, as is the case for cyanines. For donor-acceptor compounds such as **3** and **4**, polar solvents can stabilize charge separation and would increase the contribution of the charge-separated form to the ground state. Thus, donor-acceptor molecules with strong acceptors, in solvents of high polarity, would be expected to exhibit diminished bond-length alternation relative to molecules with weaker acceptors in low polarity solvents.

^{1}H nuclear magnetic resonance (NMR) (*12*), Raman (*13*), and electronic absorption (*14*) spectroscopic studies, in conjunc-

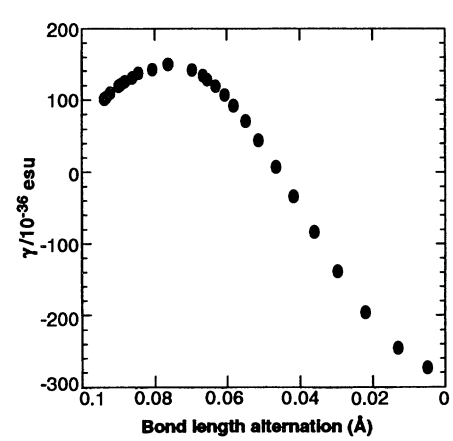

Fig. 1. Plot of γ versus <Δ*r*>, generated with an AM1 geometry optimization (in the MOPAC package) for **3** in the presence of a static electric field of varying strength (*6*). For each value of the static field, and thus <Δ*r*>, γ was calculated with a finite-field procedure; esu, electrostatic unit.

S. R. Marder, C. B. Gorman, B. G. Tiemann, Jet Propulsion Laboratory, California Institute of Technology, Pasadena, CA 91109 and The Beckman Institute, California Institute of Technology, Pasadena, CA 91125.
J. W. Perry, G. Bourhill, K. Mansour, Jet Propulsion Laboratory, California Institute of Technology, Pasadena, CA 91109.

*To whom correspondence should be addressed.